

POLARIZATION ANALYSIS OF THREE-COMPONENT ARRAY DATA

BY ANDY JURKEVICS

ABSTRACT

A technique is presented for polarization analysis of three-component seismic array data. The process is applied to a large suite of regional events recorded on the three-component sensors in the NORESS array in southern Norway. Polarization properties of the regional seismic phases P_n , S_n , and L_g are examined in detail. The analysis technique is based on a time-domain algorithm originally proposed by Flinn (1965). The polarization ellipse is computed within sliding time windows by solving the eigenproblem for the covariance matrix. Various attributes characterizing the particle motions are extracted from the motion ellipse. This technique is extended to multiple three-component sensors in an array configuration by averaging covariance matrices for the different sensors. In this case a $1/M$ reduction in the estimation variance is obtained (M is the number of sensors), when the noise and local scattering effects are uncorrelated. An important feature of this approach is that the phase velocities of coherent wavefronts across the array are not required to a high degree of accuracy. Significant results of the data analysis are the well-defined polarization of P_n and S_n waves across the entire short-period band, the source azimuth estimates obtained from P_n and L_g motions, and the distinct polarization for S_n and L_g waves allowing these phases to be distinguished in most cases.

INTRODUCTION

Three-component recordings are important for regional seismic monitoring because regional phases can exhibit large horizontal motions. Simple side-by-side displays of three-component seismograms can assist an analyst performing interpretations. However, a more quantitative approach involves processing the signals and extracting or enhancing their polarization content. There are two basic procedures which can be used for analyzing three-component data. The first involves applying some type of non-linear filter to the data based on their polarization content and outputting modified seismograms. The second involves estimating parameters of some *a priori* model fitted to the data in a time-varying manner. A partial list illustrating the variety of algorithms implemented for single-sensor three-component analysis includes Mims and Sax (1965), Flinn (1965), Simons (1968), Montalbetti and Kanasevich (1970), Smart (1977), Samson and Olson (1980, 1981), Smart and Sproules (1981), von Seggern and Marshall (1982), Christofferson *et al.* (1985), Sutton *et al.* (1987), and Magotra *et al.* (1987). These include both time and frequency domain algorithms; choice of a method generally depends on the application and the bias of the user. Comparatively little work has been done on data analysis from arrays of three-component sensors. Esmersoy *et al.* (1985) address the problem of estimating particle-motion parameters simultaneously with the wavefield slowness from three-component arrays. Kvaerna and Doornbos (1986) have implemented a similar approach and applied it to short-period data from the three-component array at NORESS. (Throughout this paper the term "sensor" is synonymous with "three-component sensor"—a seismograph installation recording three orthogonal components of motion. The term "three-component array" means multiple three-component sensors in an array configuration.)

The objective of the work described in this paper has been to implement a practical algorithm for polarization analysis which can be applied to three-component data from either single sensors or from seismic arrays. The procedure was meant to be used in both interactive "seismic workstation" and automatic on-line "post-detector" modes. After considering a variety of algorithms, a time-domain technique based on work by Flinn (1965) was chosen. Extensions to Flinn's original method include a frequency decomposition and the application to arrays of three-component sensors. Basically, the technique involves filtering the signals into a series of narrow frequency bands, applying short sliding time windows and then computing the polarization ellipse from the covariance matrix in each window in each band. Instead of polarization filtering the traces, a series of attributes describing the particle-motion characteristics as a function of time and frequency are output. Application to three-component arrays is accomplished by averaging covariance matrices for all array sensors before solving the eigenproblem.

This analysis is applied to a large suite of regional events recorded on the small-aperture NORESS array in southern Norway. A description and history of this array can be found in Mykkeltveit and Bungum (1984) and Ingate *et al.* (1985). The objective here was to exploit the signal-to-noise advantage gained by using an array to examine the polarization properties of regional seismic phases. The seismograms were processed interactively on a workstation, with an analyst carefully identifying seismic phases and selecting analysis windows. Results showed that a proper selection of the time and frequency intervals including the most purely polarized motions for a given phase was an important factor affecting the quality of results. Attributes computed for the various regional phases indicate that useful information can be obtained down to a signal-to-noise ratio (SNR) of one using only four sensors in an array, and that P_n and S_n waves have a well-defined polarization across the entire short-period band. Source azimuths can be estimated quite reliably using P_n , less so using L_g waves, and poorly with S_n . Also, results showed that S_n waves can be distinguished from L_g waves in most cases using their particle-motion characteristics. Separating S_n and L_g is particularly important since L_g times are used in regional array location programs (Mykkeltveit and Bungum, 1984) and frequency-wave number slowness estimates often fail to distinguish these secondary phases.

THEORETICAL BACKGROUND

Single three-component sensor. The processing is carried out in the time domain. Three-component seismograms are bandpass filtered into a series of narrow frequency bands as illustrated schematically in Figure 1. For each band, an identical series of overlapping, tapered time windows are applied to each component of motion. The polarization is estimated separately in each window. An assumption is made that the ground motion in each frequency band is purely polarized over the window duration. The frequency and time resolutions are controlled separately by the bandwidths and window lengths, which should be tailored to each application.

The polarization within a time window is estimated as follows. Let $\mathbf{X} = [x_{ij}]$; $i = 1, \dots, N$; $j = 1, \dots, 3$ be the data matrix in one window, where x_{ij} is the i th sample of component j and N is the number of samples. The mean for each component of \mathbf{X} over this window is taken here to be zero. The covariance matrix \mathbf{S} is evaluated as

$$S_{jk} = \frac{\mathbf{X}\mathbf{X}^T}{N} = \left[\frac{1}{N} \sum_{i=1}^N x_{ij}x_{ik} \right]$$

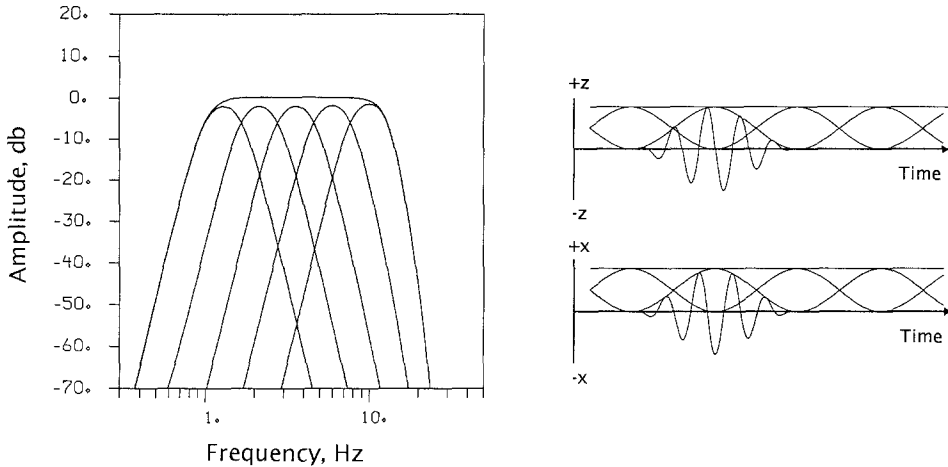


FIG. 1. Schematic illustration of the frequency and time decomposition used in the polarization analysis. The left side shows the amplitude response of a series of Butterworth bandpass filters. A summation of the individual bands yields a flat amplitude spectrum. The right side shows cosine-tapered time windows overlapping by 50 per cent and applied identically to each component of motion.

where T denotes transpose. The covariance matrix is 3×3 , real and symmetric. Explicitly, the terms of \mathbf{S} are the auto- and cross-variances of the three components of motion:

$$\mathbf{S} = \begin{bmatrix} S_{zz} & S_{zn} & S_{ze} \\ S_{zn} & S_{nn} & S_{ne} \\ S_{ze} & S_{ne} & S_{ee} \end{bmatrix}$$

where S_{zn} denotes the cross-variance of the vertical and north components, etc. (The index convention used here is $z = 1$, $n = 2$, $e = 3$.) The covariance matrix \mathbf{S} is positive semidefinite, which means the eigenvalues are real and non-negative (some may be zero). \mathbf{S} is the matrix of coefficients for a quadratic form which is an ellipsoid. This ellipsoid, termed the polarization ellipsoid, is the best fit to the data in a least-squares sense. The principal axes of the ellipsoid are found by solving the algebraic eigenproblem for \mathbf{S} . This involves finding the eigenvalues ($\lambda_1 \lambda_2 \lambda_3$) and eigenvectors ($\mathbf{u}_1 \mathbf{u}_2 \mathbf{u}_3$) which are nontrivial solutions to

$$(\mathbf{S} - \lambda^2 \mathbf{I})\mathbf{u} = 0$$

where \mathbf{I} is the 3×3 identity matrix and 0 is a column vector of zeros. The eigenvectors are chosen to be orthogonal and unit length. The three principal axes of the polarization ellipsoid are given by $\lambda_j \mathbf{u}_j$, $j = 1, \dots, 3$ where the eigenvectors are the axis orientations and their lengths are λ_j in amplitude units. The eigenproblem of a well-conditioned 3×3 symmetric matrix can be computed very quickly using standard numerical libraries such as IMSL.

The eigenvalues are ordered such that $\lambda_j \geq \lambda_k$ for $j < k$. Purely rectilinear ground motion has only one nonzero eigenvalue; $\lambda_j = 0$, $j \neq 1$. Purely elliptical polarization has two nonzero eigenvalues, $\lambda_1 \geq \lambda_2$, $\lambda_3 = 0$. In real applications, all three eigenvalues are generally nonzero and nonequal, so the polarization is ellipsoidal. The covariance matrix is found to be well-conditioned in practice because seismic noise and scattering distortions tend to be uncorrelated between the three components over a window.

Once the principal axes of the polarization ellipsoid are estimated, the particle motion in the data window is determined. Information describing the characteristics of ground motion is extracted using attributes computed from the principal axes. For example, the degree of rectilinearity is given by $1 - ((\lambda_2 + \lambda_3)/2\lambda_1)$, which is 1.0 when there is only one nonzero eigenvalue, as for pure body waves. Pure Rayleigh-wave motion is elliptical and the particle motion is confined to a plane. A measure of the degree of planarity is $1 - (2\lambda_3/(\lambda_1 + \lambda_2))$. The azimuth of P -wave propagation can be estimated from the horizontal orientation of rectilinear motion, given by the eigenvector \mathbf{u}_1 corresponding to the largest eigenvalue:

$$P_azimuth = \tan^{-1} \left(\frac{u_{21} \text{sign}(u_{11})}{u_{31} \text{sign}(u_{11})} \right)$$

where u_{j1} $j = 1 \dots 3$ are the three direction cosines of eigenvector \mathbf{u}_1 . The sign function is introduced to resolve the 180° ambiguity by taking the positive vertical component of \mathbf{u}_1 . Similarly, the apparent incidence angle of rectilinear motion, as measured from vertical, may be obtained from the vertical direction cosine of \mathbf{u}_1 :

$$P_incidence = \cos^{-1} |u_{11}|.$$

Other attributes may be computed in a similar manner.

Figure 2 shows several particle-motion attributes as a function of time for an actual seismogram. This event was a small earthquake recorded at the NORESS array in southern Norway. The epicenter was near the west coast of Norway about 450 km from the array. Figure 2 (below) shows the short-period vertical component of motion bandpassed into four frequency bands. Above are shown five attributes computed in 2-sec sliding windows. Frequencies between 2 and 16 Hz were used to compute these attributes using a "wide-band" technique which is described later in the text. Figure 2 illustrates how polarization information may be presented to a seismic analyst and also shows how attributes can help distinguish the regional seismic phases. The three-component amplitude is simply the square root of the trace of the covariance matrix in each time window. Rectilinearity is high for the P_n and P_g signals and gradually decreases down to the noise level in the P coda prior to S_n . The horizontal-to-vertical ratio is low for the P phases and high for S_n , with the L_g waves behaving similar to noise. The radial-to-transverse ratio is highest for P_g and lowest for L_g . The short-axis incidence is the angle, measured from vertical, of the shortest axis of the polarization ellipse. A later section in the text describes how this single parameter is useful for separating S_n from L_g .

Array of three-component sensors. Spatial arrays of seismic sensors are designed to enhance signal quality in certain frequency bands by exploiting the different spatial correlation properties of seismic signals, noise and local scattering effects. When multiple three-component sensors are used in arrays such as NORESS, polarization estimates can be significantly improved by combining information from the individual sensors. The technique used here for an array is to average the covariance matrices computed at the individual sensors (Jurkevics, 1986a, b). The motivation for this approach comes from the field of power spectral estimation where an "ensemble" average from multiple windows is commonly used to reduce

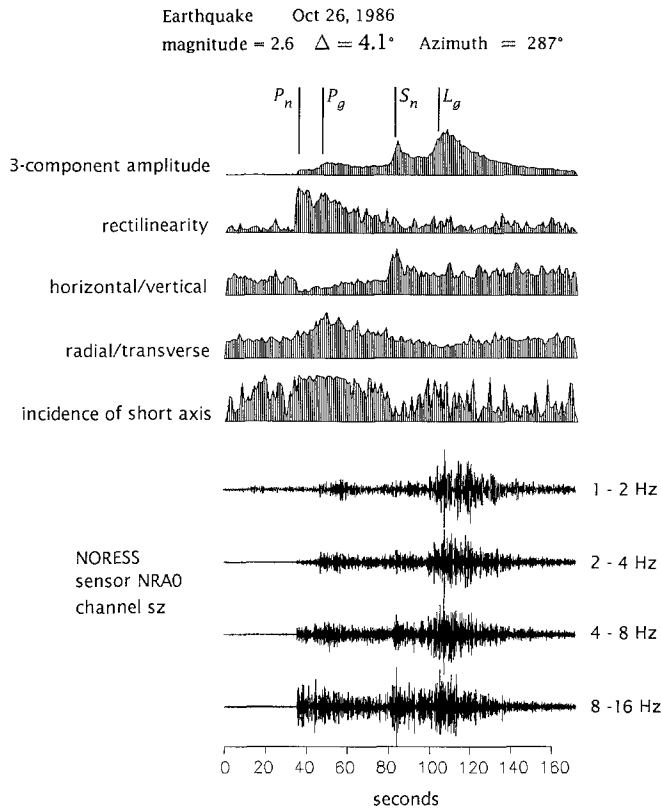


FIG. 2. *Below*, Bandpassed short-period vertical motion recorded at NORESS from a small earthquake 4.1° west of the array. *Above*, Five polarization attributes computed in 2-sec sliding time windows. This display illustrates the time-varying nature of particle motion and shows distinct polarization characteristics of the regional phases P_n , P_g , S_n , and L_g as well as the noise and coda waves. The three-component amplitude is simply the square root of the trace of the covariance matrix for each window. Simple ratios of components of motion such as horizontal-to-vertical and radial-to-transverse are useful for distinguishing different phases.

the estimation variance. For a three-component array the covariance matrix $\bar{\mathbf{S}}$ becomes

$$\bar{\mathbf{S}} = \frac{1}{M} \sum_{m=1}^M \mathbf{S}_m$$

where \mathbf{S}_m is the covariance for sensor m and M is the total number of three-component sensors. Time shifting to align the computation windows for the moveout of coherent energy across the array may be done first.

This covariance-averaging procedure is justified as follows. The individual terms of the covariance matrix \mathbf{S} are simply the (zero-lag) auto- and cross-variances between the components of motion taken over a short window. Estimation theory (Oppenheim and Schaffer, 1975) states that the (zero-lag) sample variance σ_x^2 of a stationary random signal is unbiased and consistent; i.e., σ_x^2 converges to its true value as N increases and the estimation variance of σ_x^2 goes as $1/N$, where N is the number of samples used. The sample variance can be equivalently computed by dividing the signal into a series of nonoverlapping time windows and averaging the

individual window variances. For a zero-mean signal:

$$\begin{aligned} \sigma_x^2 &= \frac{1}{N} \sum_{i=1}^N x_i^2 \\ &= \frac{1}{M} \sum_{m=1}^M \left(\frac{1}{L} \sum_{i=(m-1)L+1}^{mL} x_i^2 \right) \\ &= \frac{1}{M} \sum_{m=1}^M \sigma_{x,m}^2 \end{aligned}$$

where $N = ML$. Here M is the number of windows, each of length L , x_i is the i th data sample, and $\sigma_{x,m}^2$ is the sample variance computed over the m th window. When several independent and uncorrelated signal realizations are available, then the time-window average can be replaced by an ensemble average. In the case of polarization estimation, when the noise and local scattering effects are uncorrelated between array sensors, averaging covariance matrices between sensors corresponds to ensemble averaging. Thus the estimation variance goes as $1/M$, where M is the number of sensors in the array. The averaged covariance matrix $\bar{\mathbf{S}}$ is positive semidefinite since its symmetry is assured by the symmetry of the individual covariance matrices used in forming the sum.

Synthetic example. Figure 3 shows an example of covariance averaging using synthetic seismograms. Three-component data consisting of 5-Hz sine-wave signals with additive noise were generated. The underlying signal particle motion is rectilinear, stationary and oriented at an azimuth of 45° and an incidence angle of 30° from vertical. The noise was computed as a random-number series bandpassed

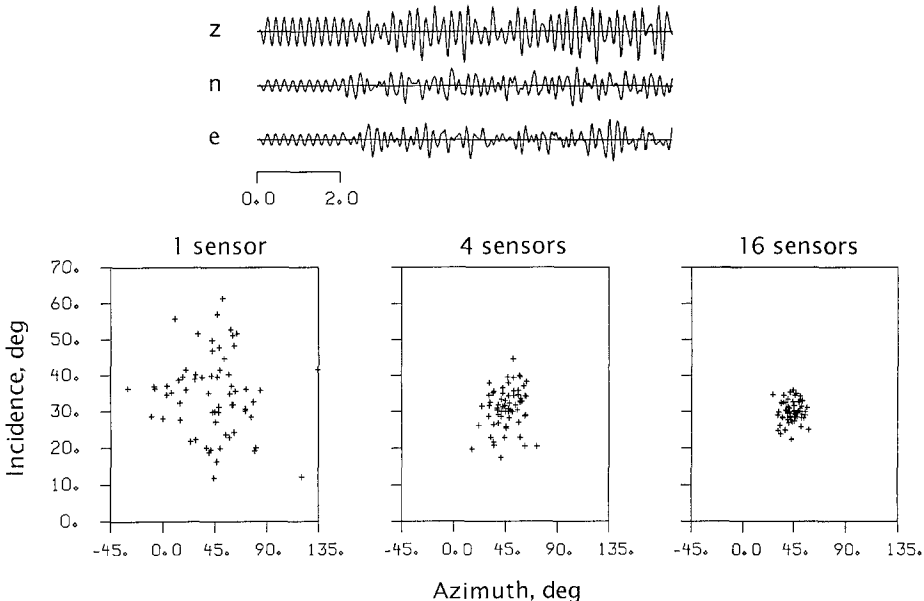


FIG. 3. The three-component array analysis applied to synthetic data. The input traces at the top consist of a 5-Hz sine-wave signal with additive noise. The signal corresponds to rectilinear particle motion with an azimuth of 45° and an incidence angle of 30° from vertical. The estimated orientation of rectilinear motion within 66 time windows using 1, 4, and 16 sensors in an array configuration is shown below. The estimation variance goes as $1/M$ where M is the number of array sensors used.

between 2 and 8 Hz. An equal amount was added to all three components. The top part of Figure 3 shows a portion of the seismograms for one sensor. The noise has been applied beginning at 2 sec to illustrate the underlying signals and the signal-to-noise level. The performance of the covariance averaging technique was tested by constructing 1, 4, and 16 realizations of such three-component seismograms corresponding to different numbers of sensors within an array. The estimated rectilinear particle motion orientations for 66 nonoverlapping one-second time windows are plotted at the bottom of Figure 3. The scatter in the computed attributes decreases with increasing number of sensors in the array. The variance in both the incidence and azimuth values in this example is proportional to $1/M$, where M is the number of sensors.

IMPLEMENTATION

Time alignment between array sensors. In order to carry out the covariance averaging it is necessary to time-align the computation windows according to the phase velocities of coherent wavefronts across the array. Results of a frequency-wavenumber analysis can be used for this. However, the time shifts are not required to nearly the same degree of accuracy as needed in beamforming. To illustrate this point, the misalignment between elements of any frequency component in beamforming must be less than about $T/5$, where T is the period, to ensure constructive phase superposition. Averaging covariance matrices requires only that the computation windows for the sensors have a substantial overlap, say better than $\frac{2}{3}$ the window length. In practice, these computation windows include at least 5 periods of the analysis frequency. If a window misalignment of $\frac{1}{3}$ is acceptable then the time-alignment accuracy must be better than $5T/3$. Thus the time alignment for beamforming must be at least eight times more accurate than for covariance averaging. If the ground motion is relatively stationary so that longer windows can be used, which is often the case at higher frequencies, then the time alignment for the covariance averaging becomes even less critical. Tests using regional seismograms recorded on the NORESS C-ring (1.5 km diameter) have shown that the covariance averaging can be satisfactorily carried out in most cases over the entire short-period band, i.e., to 15 Hz, without time shifting the windows at all.

Note that the method of covariance averaging is very different from first beamforming the three components of motion and then doing a single-sensor three-component analysis. Beamforming first yields cross terms in the covariance matrix between $sensor_1:component_j$ and $sensor_2:component_k$, etc. which are not present if the covariance is evaluated separately at each sensor. Particle-motion estimates are very sensitive to timing errors between the components of motion, so beamforming first requires a very accurate time alignment between sensors. The required accuracy increases with frequency and is difficult to obtain at higher frequencies because of local earth heterogeneities which introduce random time shifts between array elements.

Time and frequency decomposition. Seismic signals are nonstationary and band-limited. The quality of particle-motion information obtained for a given arrival depends critically on the positioning of the analysis window and choice of frequency interval. The choice of both window length and bandwidth are subject to the usual trade-offs between resolution and estimation variance. Short windows and narrow bands are required to avoid smearing information between close arrivals and to capture the frequency-varying properties of polarization. However, longer windows

TABLE 1
EVENTS USED IN THE ANALYSIS

Yr/Day of Yr	Mo-Day Time	Lat (deg)	Lon (deg)	Distance (deg)	Azimuth (deg)	Magnitude	Type*
85/213	08-01 11:17:35	45.82	26.65	17.35	142.46	4.7	E
85/298	10-25 12:03:47	59.30	28.10	8.38	92.62	2.3	X
85/300	10-27 04:36:43	61.12	4.92	3.24	279.62	2.8	E
85/312	11-08 14:18:54	58.34	6.43	3.53	229.41	2.4	X
85/313	11-09 14:42:46	57.80	7.20	3.68	218.91	2.1	X
85/313	11-09 18:20:48	62.00	7.70	2.23	306.08	2.0	?
85/317	11-13 16:32:10	58.30	6.40	3.57	229.13	1.8	X
85/317	11-13 12:07:48	59.30	28.10	8.38	92.62	2.3	X
85/324	11-20 22:10:44	57.61	5.67	4.34	226.41	2.3	u
85/324	11-20 22:24:38	57.66	5.72	4.28	226.58	2.2	u
85/324	11-20 22:57:10	57.64	5.62	4.33	226.94	2.3	u
85/324	11-20 23:10:47	57.66	5.35	4.42	228.51	2.3	u
85/324	11-20 23:17:28	57.69	5.49	4.34	228.06	2.3	u
85/324	11-20 23:23:10	57.50	5.62	4.44	225.73	2.2	u
85/324	11-20 23:28:23	57.58	5.49	4.42	227.09	2.2	u
85/325	11-21 14:18:13	59.80	8.20	1.90	241.88	1.4	x
85/325	11-21 14:48:07	54.80	6.50	6.52	206.51	2.8	x
85/325	11-21 09:16:30	58.37	12.36	2.41	169.70	—	?
85/327	11-23 13:06:18	59.50	25.00	6.81	94.59	2.1	X
85/331	11-27 04:53:32	59.73	5.71	3.06	253.31	2.8	E
85/344	12-10 12:05:39	59.40	28.50	8.54	91.57	2.2	X
85/357	12-23 02:35:08	60.38	1.90	4.75	269.87	2.3	E
85/358	12-24 12:37:57	59.80	22.50	5.51	95.02	1.9	?
85/359	12-25 13:19:01	58.70	26.00	7.55	99.30	2.6	?
85/361	12-27 12:16:08	59.40	28.50	8.54	91.57	2.4	X
85/365	12-31 06:57:17	73.31	6.62	12.71	353.57	4.8	E
86/003	01-03 14:58:41	61.90	30.60	9.19	74.46	2.5	X
86/007	01-07 14:14:28	58.34	6.43	3.53	229.41	2.2	X
86/009	01-09 09:18:43	54.70	19.50	7.37	141.43	2.7	?
86/017	01-17 14:11:01	58.34	6.43	3.53	229.41	2.3	X
86/019	01-19 04:59:22	65.00	12.13	4.27	3.35	3.0	E
86/020	01-20 23:38:28	50.19	12.37	10.56	177.10	4.9	?
86/021	01-21 08:55:40	55.30	13.60	5.55	167.78	2.5	?
86/031	01-31 12:10:15	59.30	28.10	8.38	92.62	3.2	X
86/035	02-04 12:14:59	59.50	26.50	7.54	92.90	2.8	X
86/035	02-04 12:58:59	59.40	24.60	6.64	95.91	2.5	X
86/035	02-04 14:22:57	59.30	24.40	6.57	97.00	2.6	X
86/036	02-05 17:53:16	62.81	4.86	3.77	306.15	4.7	E
86/037	02-06 16:29:55	67.10	20.60	7.49	28.05	2.7	X
86/037	02-06 12:22:04	59.30	28.10	8.38	92.62	2.7	X
86/038	02-07 14:06:11	***	***	3.80	210.00	1.6	?
86/038	02-07 11:00:01	64.70	30.70	9.58	57.40	3.1	X
86/038	02-07 14:05:22	***	***	3.80	210.33	2.8	?
86/041	02-10 12:41:46	59.40	28.50	8.54	91.57	2.5	X
86/045	02-14 14:13:19	58.34	6.43	3.53	229.41	2.4	X
86/045	02-14 17:54:04	58.34	6.43	3.53	229.41	2.3	X
86/045	02-14 12:10:21	59.40	28.50	8.54	91.57	2.7	X
86/045	02-14 16:44:08	67.10	20.60	7.49	28.05	2.6	X
86/049	02-18 10:46:16	59.30	27.20	7.94	93.57	2.6	X
86/049	02-18 12:45:50	64.70	30.70	9.58	57.40	2.6	X
86/057	02-26 02:11:44	62.76	5.29	3.58	307.05	2.5	E
86/062	03-03 07:26:06	43.70	31.40	20.76	136.13	4.4	E
86/064	03-05 14:16:31	66.30	21.70	7.15	34.70	—	?
86/064	03-05 12:13:19	59.50	26.50	7.54	92.90	2.6	X
86/064	03-05 13:02:05	60.63	2.58	4.38	272.47	2.1	E

TABLE 1—continued

Yr/Day of Yr	Mo-Day Time	Lat (deg)	Lon (deg)	Distance (deg)	Azimuth (deg)	Magnitude	Type*
86/067	03-08 16:21:17	61.67	2.58	4.41	286.06	2.4	E
86/069	03-10 12:02:09	59.30	28.10	8.38	92.62	2.6	X
86/069	03-10 04:20:04	62.81	4.91	3.75	306.32	2.5	E
86/070	03-11 12:02:28	59.30	28.10	8.38	92.62	2.6	X
86/071	03-12 11:07:21	59.50	26.50	7.54	92.90	2.5	X
86/071	03-12 12:01:38	59.40	28.50	8.54	91.57	2.5	X
86/078	03-19 12:06:40	59.40	28.50	8.54	91.57	2.6	X
86/089	03-30 03:22:37	61.66	4.53	3.50	288.29	2.2	E
86/091	04-01 09:56:53	56.42	12.10	4.33	175.89	3.6	E
86/094	04-04 22:42:30	71.08	8.35	10.42	354.27	4.6	E
86/097	04-07 00:34:37	61.84	4.88	3.38	291.88	2.3	E
86/108	04-18 00:44:13	59.22	1.42	5.28	257.72	2.4	E
86/114	04-24 09:53:12	***	***	1.50	200.00	—	?
86/133	05-13 09:23:44	***	***	4.30	115.00	4.5	?
86/154	06-03 14:30:04	61.46	4.08	3.67	284.54	2.8	E
86/155	06-04 09:06:31	61.50	30.40	9.11	77.00	3.3	X
86/163	06-12 09:30:55	61.50	30.40	9.11	77.00	3.1	X
86/166	06-15 15:01:07	61.67	3.85	3.82	287.44	3.0	E
86/168	06-17 12:12:07	59.40	28.50	8.54	91.57	2.6	X
86/169	06-18 11:05:08	59.40	28.50	8.54	91.57	2.5	X
86/170	06-19 03:55:08	59.31	6.54	2.88	242.39	2.4	X
86/171	06-20 22:07:53	61.47	3.92	3.75	284.53	2.0	?
86/177	06-26 04:06:21	61.88	5.10	3.29	293.05	2.4	E
86/178	06-27 03:49:46	59.28	6.76	2.80	240.66	2.5	E
86/185	07-04 11:13:27	59.30	28.10	8.38	92.62	2.6	X
86/195	07-14 13:50:32	58.35	13.82	2.65	153.21	4.0	E
86/195	07-14 14:30:27	61.10	29.90	8.90	79.67	2.9	X
86/195	07-14 15:02:19	69.30	34.40	12.76	38.43	2.9	X
86/222	08-10 05:01:04	59.99	5.34	3.15	258.96	1.7	E
86/228	08-16 04:24:36	62.82	4.98	3.73	306.70	2.5	E
86/244	09-01 22:11:26	60.82	2.93	4.20	274.85	3.5	E
86/273	09-30 20:02:47	60.79	4.23	3.57	273.99	2.4	E
86/283	10-10 19:56:31	61.97	2.33	4.58	289.58	2.3	E
86/299	10-26 11:45:06	61.46	3.29	4.05	283.83	2.6	E
86/299	10-26 11:57:03	61.72	3.27	4.10	287.43	2.6	E
86/302	10-29 21:05:01	60.81	3.04	4.15	274.68	2.4	E
86/327	11-23 03:30:32	73.74	9.08	13.03	356.94	4.7	E
86/346	12-12 16:33:30	72.96	4.80	12.49	350.85	4.7	E

* X = explosion, x = presumed explosion, E = earthquake, e = presumed earthquake, ? = unknown source type, u = presumed underwater explosion.

*** Location based on frequency-wavenumber analysis only.

and wider frequency bands yield more stable and reliable estimates. The nature of the signals being processed as well as the objectives of the particular analysis must determine the resolution settings.

In real seismograms the signal amplitude level, signal-to-noise ratio and polarization characteristics all vary with frequency. In this algorithm, frequency decomposition involves applying a bank of narrow-band filters as shown schematically in Figure 1. Short-order recursive Butterworth filters are used so the bandpassing is very fast. The frequency bands were chosen to be one octave wide, although fixed bandwidths can also be used. The computation time windows are cosine tapered and overlapped by 50 per cent. The window lengths can be fixed or vary with

frequency. The rationale for varying the window length is that higher frequencies inherently yield a shorter time resolution than do lower frequencies. Data analyses so far have shown that purely polarized motions for most short-period phases generally last no more than a few seconds, so the window lengths should be between about 0.5 and 5 sec. An exception to this is the L_g wavetrain, which is longer duration and relatively stochastic by nature, so longer computation windows tend to give more stable results.

Wide-band estimate. When detailed frequency dependence of polarization is not required the most stable estimates are obtained by using wide bands. However, since signal amplitudes vary strongly with frequency, using a single wide frequency band will result in the frequency component at the peak amplitude dominating the polarization estimate. For this reason some kind of spectral balancing is needed. This is accomplished by computing separate covariance matrices in a series of narrow frequency bands, normalizing them and then averaging. The time windows are constructed identically in each band. The trace of the covariance matrix is used as the normalization factor. An individual covariance matrix \mathbf{S}^k for the k th band is computed in the usual way, and the wide-band estimate obtained by

$$\bar{\mathbf{S}} = \left(\sum_{k=1}^K \text{trace}(\mathbf{S}^k) \right) \sum_{k=1}^K \frac{\mathbf{S}^k}{\text{trace}(\mathbf{S}^k)}$$

where K is the number of bands to include. The polarization attributes displayed in Figure 2 were computed using such a wide-band procedure combining the three frequency bands 2 to 4, 4 to 8, and 8 to 16 Hz.

APPLICATION TO REGIONAL SEISMOGRAMS AT NORESS

Description of data. The analysis procedure described above was applied to a large suite of regional seismograms recorded at NORESS. A total of 93 events is contained in this dataset. Of these, 41 are earthquakes, 40 are mining explosions and the remainder are unknown source types. All of the events occurred within a distance of 21° of NORESS and had reported magnitudes less than 5.0. The locations, magnitudes and source types for most of these events were obtained from local bulletins. Most of the magnitude values are based on coda duration. Some of the events were chosen from Preliminary Determination of Epicenters (PDE) listings with reported magnitudes as m_b . Thus, there is some inherent mixing of magnitude scales. The events were selected to have a range of signal-to-noise levels in order to study the effects of noise on polarization. A majority of the events fall into three clusters—a series of mining explosions and presumed underwater explosions near the south coast of Norway southwest of the array and at a distance of about 3.5° to 4.0° , a series of mining explosions to the east at a distance of about 8.0° to 9.0° , and a series of earthquakes west of the array at a distance of about 3.0° to 5.0° . Table 1 contains a listing of events used. Figure 4 shows the locations of the epicenters as well as the NORESS array geometry. A number of the events are co-located and so their symbols overlap in Figure 4.

Analysis procedure. The analysis of the regional seismograms was performed interactively using a workstation. Three frequency bands were used, each one octave wide and centered at 4 Hz (2.7 to 5.3 Hz), 6 Hz (4 to 8 Hz), and 10 Hz (6.7 to 13.3 Hz). Fixed frequency bands, as opposed to variable frequency intervals based on the SNR versus frequency, were used so the particle-motion characteristics could

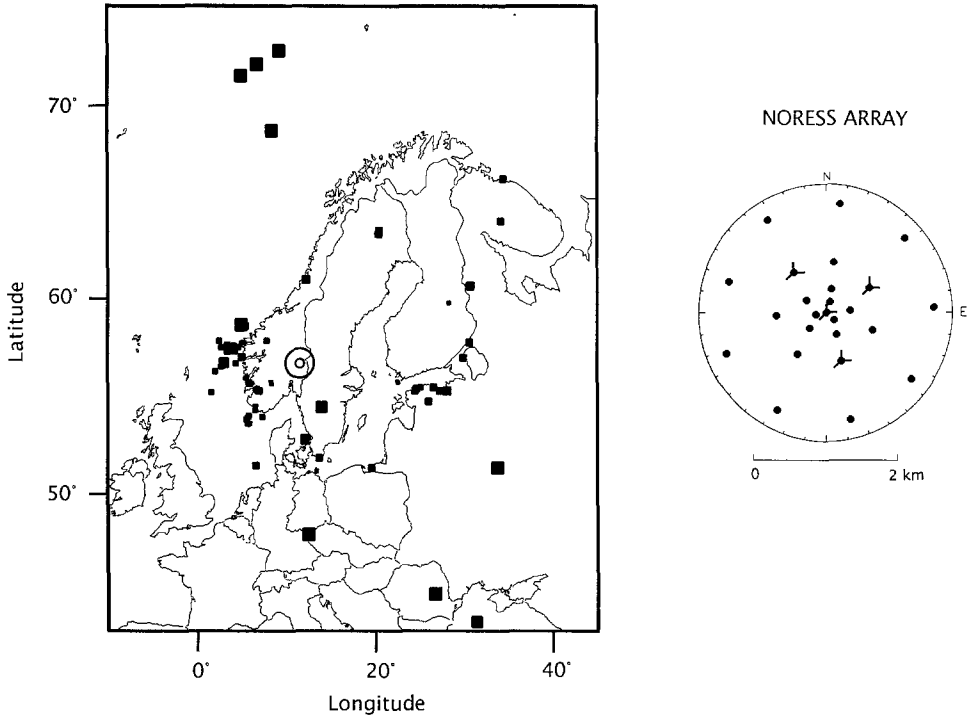


FIG. 4. Map of the Scandinavia region showing epicenters of the events used in the analysis. The symbol size is proportional to magnitude. A number of the events are associated with the same source and are co-located. Geometry of the small-aperture NORESS array including the four three-component sensors is also shown.

be studied as a function of frequency. The time resolution (i.e., short computation window length) was set to five cycles of each passband center frequency. For most of the events used in this analysis the NORESS array contained four three-component sensors—three on the “C” ring (diameter = 1.5 km) and one sensor at the center. No time shifting was used to align the time windows between the sensors to compensate for the time lags of the wavefronts across the array. Tests using a subset of these events showed that the difference between a simple zero-lag covariance summation and a time-shifted summation based on the frequency-wavenumber solution is negligible in most cases.

The particle-motion attributes were extracted at time picks selected by the analyst. A series of attributes were computed and displayed as a function of time to assist in choosing the extraction time interval for each phase. The sliding computation windows were made quite short (five cycles) in order to give a high resolution display of the time-varying polarization content. The attributes were extracted over time intervals which always included several of the short computation windows used to evaluate the covariance matrices. The polarization attributes from neighboring computation windows were simply averaged together and output to a file. This procedure allowed the extraction interval to vary in length according to the duration of purely polarized motion for each phase. Table 2 shows the extraction window lengths used. The best particle-motion information for any arrival is generally between the onset time and shortly after the peak amplitude. The ambient noise sample was taken prior to the P_n arrival. P_n attributes were taken over a 2-sec window at the time the signal amplitude and rectilinearity were largest. The

TABLE 2
EXTRACTION WINDOW LENGTHS

Phase	Extraction Window
Noise	6 sec
P_n	2 sec
Late P coda	6 sec
S_n	Selected by analyst
L_g	Selected by analyst

noise level for S_n and L_g was taken from the late P coda just prior to the onset of S_n . The S_n and L_g windows were based on the shapes of the three-component envelopes and included the time durations over which the three-component amplitudes are above about 40% of their peak values. The extraction windows were typically 3 to 8 sec for S_n and 10 to 20 sec for L_g .

RESULTS

Figure 5 shows the rectilinearity and incidence angle of rectilinear motion for ambient noise and P_n waves. The values for noise are plotted at a SNR of 1.0. The P -wave rectilinearity is about equal to the noise rectilinearity when SNR = 1.0 and generally increases with increasing SNR. The incidence angle is simply the orientation, measured from vertical, of the eigenvector corresponding to the largest eigenvalue. The P_n waves with signal-to-noise levels above about 3.0 in Figure 5 show a decrease in incidence angle with increasing frequency. The average values vary from about 45° at 4 Hz to about 30° at 10 Hz. Although not shown here, there was no obvious correlation between the rectilinear incidence angle and source distance for the P_n waves.

A common application of three-component analysis is to estimate source azimuth. Figure 6 shows the error in estimated source azimuth using P_n and L_g particle motion as determined in this study. S_n waves did not yield reasonable azimuth estimates. The values plotted in Figure 6 are the true station-to-epicenter azimuths minus the back azimuths from the particle motions. The P_n azimuth was computed as simply the horizontal orientation of the eigenvector corresponding to the largest eigenvalue of the covariance matrix. There is a decrease in the P_n azimuth errors as the signal-to-noise level increases. Taking the data for all noise levels, one standard deviation in the azimuth error for P_n is 10°, 12°, and 14° for the 4, 6, and 10 Hz bands, respectively. The variance could be further reduced by combining the covariance matrices from the frequency bands for which SNR > 1.0 into a single wide-band estimate. L_g source azimuths were computed by the method of von Seggern and Marshall (1982) who used the orientation of the minimum horizontal motion of L_g wavetrains. Figure 6 shows the errors in source azimuth using the minimum horizontal motion of L_g . This value was computed as the orientation of the eigenvector corresponding to the smallest eigenvalue computed from the two horizontal components. There is a ±180° ambiguity in this azimuth. The values plotted in Figure 6 were computed using the sign which gave the smallest error.

In contrast to P_n , the L_g azimuth errors are a strong function of frequency. One standard deviation is 16°, 27°, and 36° for the 4, 6, and 10 Hz bands, respectively. Thus the L_g azimuths are not as accurate as those estimated from P_n motions. The skewed distribution of points in Figure 6 particularly visible at 10 Hz is correlated with source location. The cluster of points at 10 Hz with low SNR values and

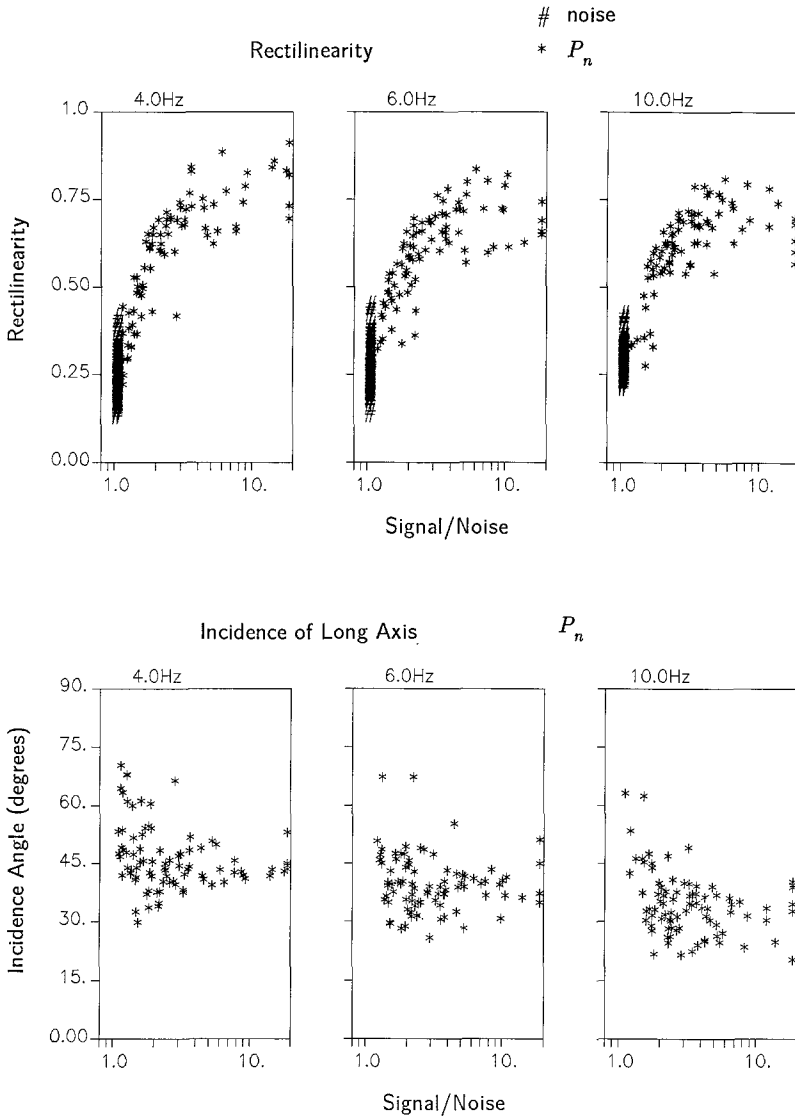


FIG. 5. Above, Rectilinearity of P_n as a function of SNR in three frequency bands. Below, apparent angle of incidence computed from the orientation of the rectilinear P_n motion. The scatter is a function of the SNR and the average incidence angle tends to decrease with increasing frequency.

positive errors are all from mining explosions 800 to 900 km east of NORESS. These waves appear to be arriving at the array from a more southerly direction than the true azimuth. This is likely due to geologic inhomogeneities along the propagation paths.

The upper part of Figure 7 shows the vertical-to-horizontal amplitude ratios of the noise, P_n , S_n , and L_g . The vertical-to-horizontal ratio is computed as $2Z/(E + N)$, with the factor of 2 introduced simply to normalize the values to 1.0 when all components are equal. The noise, which is plotted at SNR = 1, has an average V/H value slightly less than 1.0. P_n waves are clearly distinct from the other phases. Their V/H values increase with increasing SNR. The fact that the vertical-to-horizontal ratios for P_n increase with frequency is consistent with the P_n incidence

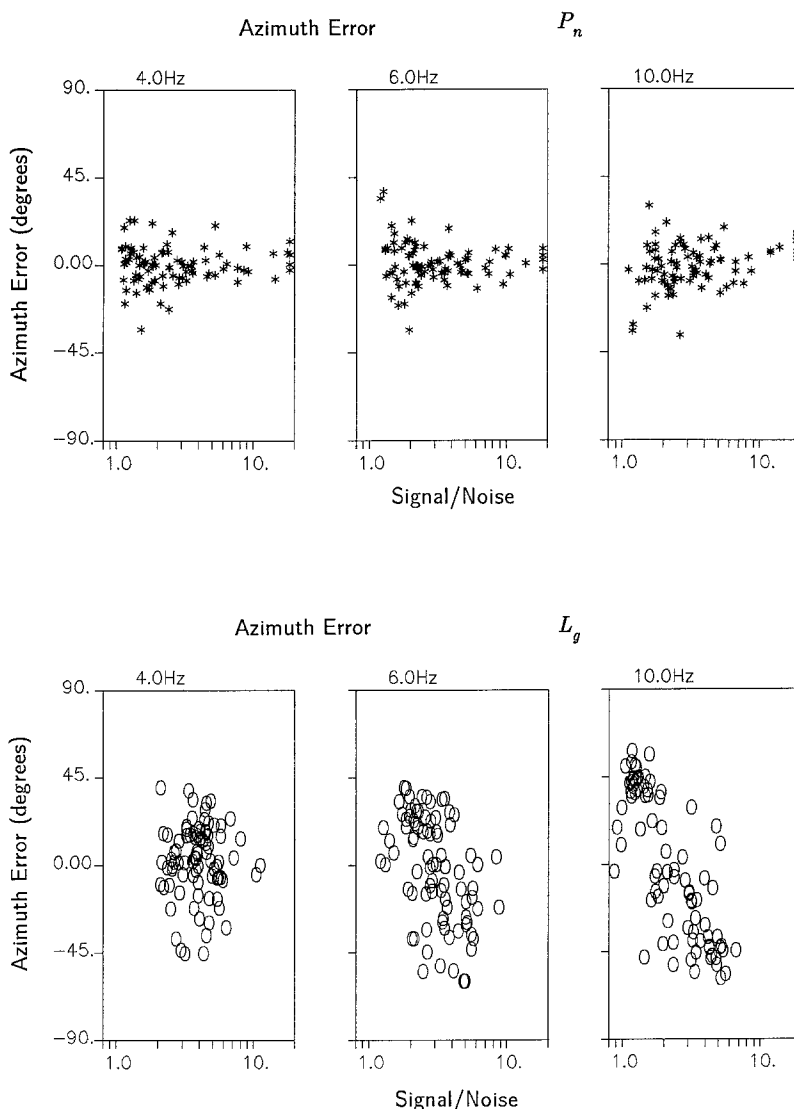


FIG. 6. *Above*, Source azimuth error computed from the orientation of the longest principal axis for P_n motion. One standard deviation using the data for all SNR values is 10° , 12° , and 14° for the 4, 6, and 10 Hz bands, respectively. *Below*, Source azimuth error for L_g computed from the orientation of the shortest principal axis using the horizontal components. The error increases with frequency and the asymmetric grouping at 10 Hz is a path effect.

angles in Figure 5. S_n waves have considerably smaller vertical motions compared with the horizontals. The V/H values for S_n tend to decrease with increasing SNR, and are very well separated from the noise at 10 Hz. L_g waves have vertical-to-horizontal ratios which cluster tightly at 4 and 6 Hz and are similar to the values for noise. Some of the overlap between S_n and L_g at 10 Hz is due to the lack of high-frequency components in the L_g wavetrain, so the signals on the seismograms at the L_g pick times at 10 Hz are actually late S_n coda (Ringdal, 1986).

The lower part of Figure 7 shows the radial-to-vertical (R/V) ratios for S_n , L_g and noise. S_n waves have radial motions considerably larger than verticals at all frequencies. L_g motions, on the other hand, have radials smaller than verticals at 4 and 6 Hz. At 10 Hz the L_g motions are similar to the noise, and some L_g waves even

have $R/V > 1$. Again, this is because of L_g attenuation at higher frequencies so the information at the L_g pick times is actually taken from late S_n coda.

The upper part of Figure 8 shows the relative amplitudes of the radial and transverse (R/T) motions for noise, S_n and L_g . The noise values, plotted at SNR = 1, have a mean of about 1.0 and a considerable scatter. (Note the different scales used on the y-axes for the plots in Figures 7 and 8). The S_n waves have R/T values very similar to those of noise. The L_g waves have radial motions which are consistently smaller than the transverse motions at lower frequencies. This property was previously used to obtain the source azimuths from L_g waves.

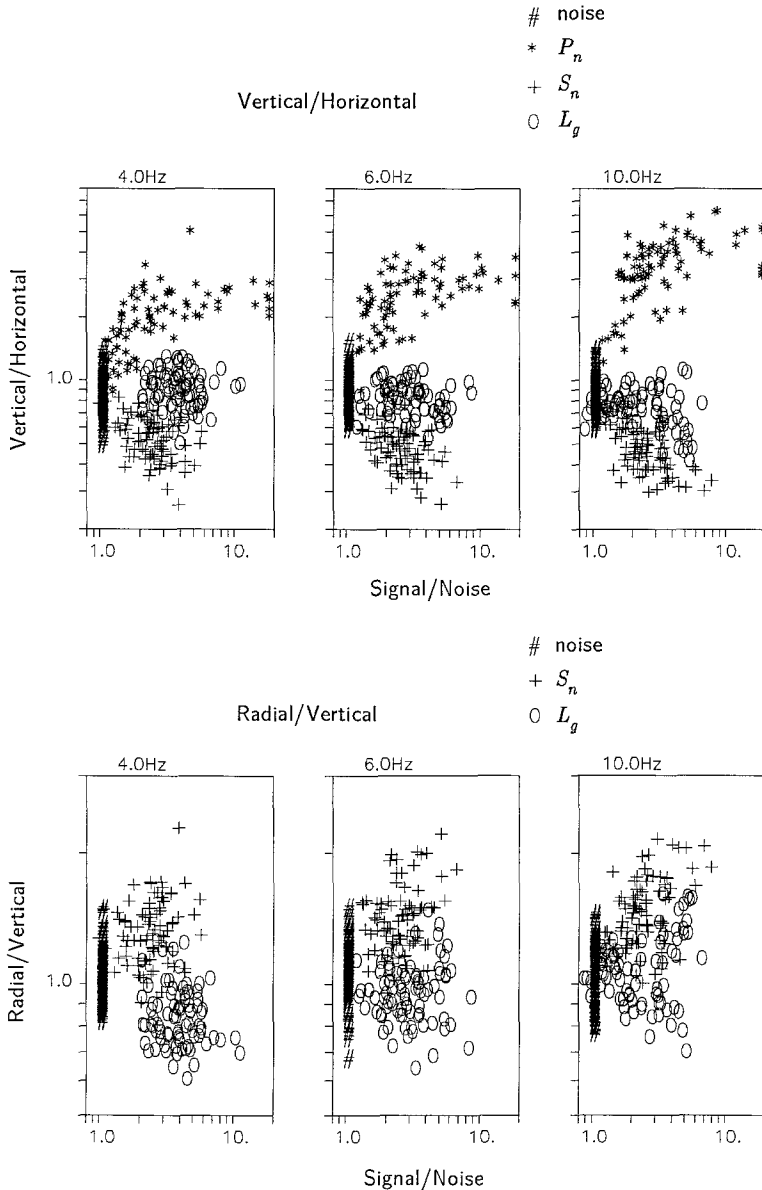


FIG. 7. Above, Vertical-to-horizontal ratios of motion for the various phases. The values plot at $V/H = 1.0$ when all components are equal. Both P_n and S_n ratios differ significantly from 1.0 for high signal-to-noise levels. Below, Ratios of radial and vertical components for noise, S_n and L_g . S_n waves tend to have larger radials than verticals at all frequencies. L_g waves have smaller radials at lower frequencies.

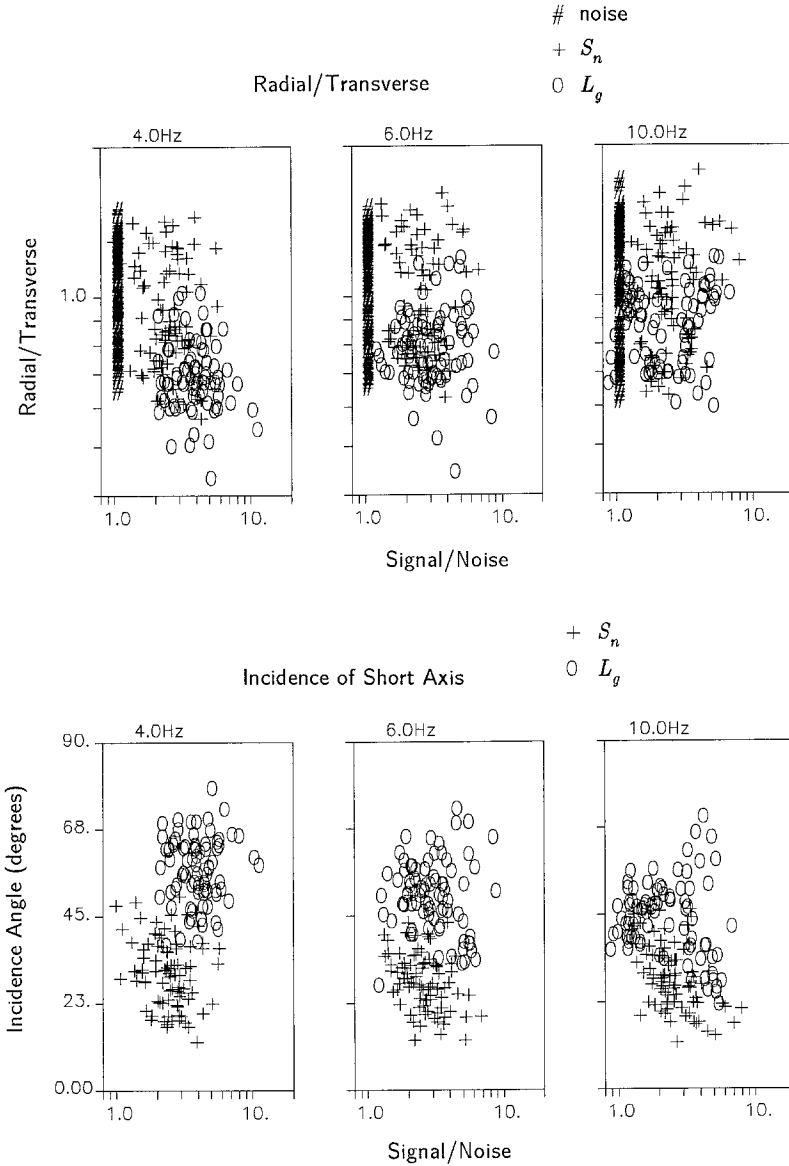


FIG. 8. Above, The radial-to-transverse motions of S_n are similar to those of noise and about 1.0 on the average. Radial motions of L_g at low frequencies are smaller than transverse motions. Below, The orientation of the shortest principal axis of the polarization ellipsoid indicates the orientation of the dominant plane of motion. The dominant plane of motion for S_n is closer to horizontal and for L_g it is closer to vertical.

The plots V/H , R/V , and R/T suggest that the particle motions for both S_n and L_g tend to be relatively planar by nature, but that the orientation of this plane of motion is different for these phases. S_n motions are dominantly horizontal, with radial amplitudes equal to transverse on the average. L_g motions are dominant in a vertical plane perpendicular to the source azimuth, with transverse and verticals about equal and radials smaller. The lower part of Figure 8 shows one parameter which characterizes the orientation of the plane of dominant motion for S_n and L_g . This parameter is the incidence angle, measured from vertical, of the eigenvector

for the smallest eigenvalue. This eigenvector is the perpendicular to the dominant plane of ground motion. An incidence angle close to 0° indicates the plane of motion is dominantly horizontal. A value close to 90° means the plane of motion is nearly vertical. There is a good separation between S_n and L_g using this one parameter. It reflects what was described previously, namely that the S_n motions are dominantly horizontal at all frequencies and that the L_g plane of motion at lower frequencies tends to be closer to vertical. These results suggest that S_n seismic waves are incident at about 20° to 35° from vertical at NORESS and contain both S_H and S_V waves. Similarly, the L_g waves appear to contain both S_H and S_V components and are incident at about 50° to 70° from vertical. Using the short-axis incidence angle attribute to separate these phases is more convenient than the radial-to-vertical ratio since the source azimuth is usually unknown ahead of time.

CONCLUSIONS

A technique for computing particle-motion information using three-component seismograms from either single sensors or arrays has been outlined. The use of an array of three-component sensors was found to reduce the estimation variance of polarization attributes by $1/M$, where M is the number of sensors, when the noise and scattering distortions are uncorrelated between sensors. The method was applied to 93 regional events recorded on the three-component sensors in the NORESS array. Attributes were extracted from time windows picked interactively by an analyst. The array processing resulted in stable polarization estimates for the regional phases which would be difficult to obtain from single-sensor recordings because of interference from noise and local scattering. The following conclusions can be drawn from this study:

1. S_n signals have a distinctive polarization allowing them to be distinguished from the other regional phases in most cases. The radial and transverse components of S_n tend to be about equal and greater than the vertical components.
2. L_g waves have a distinct polarization (at lower frequencies) by which they can be distinguished from the other phases in most cases. L_g motions tend to have smaller radial components and about equal vertical and transverse motions. L_g polarization is less reliable at higher frequencies, apparently because the high-frequency signals often consist of late S_n coda, not L_g waves.
3. P_n and S_n phases have well-defined polarization up to at least 13 Hz (the upper frequency used in this analysis) whenever there is signal above noise at these frequencies.
4. The quality of polarization information deteriorates with increasing noise level. However, when multiple three-component elements are used in an array (four sensors in this case), then the polarization attributes are informative for signal-to-noise levels down to 1.0.
5. Using four three-component sensors of the NORESS array, azimuth from P_n motions can be estimated with a standard deviation of about 10 to 12° . L_g azimuths can be estimated from the minimum horizontal motions but are not as accurate as P_n azimuths. Tests with synthetic signals indicate these results would be improved by the addition of more three-component sensors.

The analysis procedure outlined can be implemented in either an interactive seismic workstation or an automatic on-line processing system. The algorithm works in the time domain and is very fast, so polarization characteristics may be computed continuously in real time. Thus the choice of time windows and frequency

intervals for extracting polarization information can be made on the basis of the computed attributes themselves. This is important because the quality of the extracted information depends on situating the time windows on the purest particle motions, which are generally of short duration. In an interactive mode, the analyst simply examines time histories of polarization attributes in several frequency bands and selects the bands and windows with the best motions. In automatic mode, the amplitudes in several bands can be compared with the ambient noise levels in these bands. The frequency interval is then chosen for which the SNR is above some threshold. Seismic phases for a given region can be identified by comparing attributes computed for an unknown arrival with a table of values obtained from a controlled study such as this one.

ACKNOWLEDGMENTS

Helpful discussions with Paul Dysart and Robert Blandford are acknowledged. This work was part of an effort to develop seismic processing capabilities for Sun workstations at the Center for Seismic Studies. This research was supported by the Defense Advanced Research Projects Agency through the Defense Supply Service-Washington under contract No. MDA903-84-C-0020.

REFERENCES

- Christoffersson, A., E. S. Husebye, and S. F. Ingate (1985). A new technique for 3-component seismogram analysis, Semiannual Technical Summary, Oct. 1984–Mar. 1985, NORSAR Scientific Report 2-85/86, Kjeller, Norway.
- Esmersoy, C., V. F. Cormier, and M. N. Toksoz (1985). Three-component array processing, in *The VELA Program. A Twenty-Five Year Review of Basic Research*, A. U. Kerr, editor, DARPA, Arlington, Virginia.
- Flinn, E. A. (1965). Signal analysis using rectilinearity and direction of particle motion, *Proc. IEEE* **53**, 1874–1876.
- Ingate, S. F., E. S. Husebye, and A. Christoffersson (1985). Regional arrays and optimum data processing schemes, *Bull. Seism. Soc. Am.* **75**, 1155–1177.
- Jurkevics, A. (1986a). Polarization analysis using an array of three-component sensors: Part I—theory, SAIC Quarterly Technical Report for July–September 1986, Center for Seismic Studies Technical Report C86-07, Arlington, Virginia.
- Jurkevics, A. (1986b). Polarization analysis using an array of three-component sensors: Part II—application to NORESS, SAIC Quarterly Technical Report for July–September 1986, Center for Seismic Studies Technical Report C86-07, Arlington, Virginia.
- Kvaerna, T. and D. J. Doornbos (1986). An integrated approach to slowness analysis with arrays and three-component stations, Semiannual Technical Summary, October 1985–March 1986, NORSAR Scientific Report 2-85/86, Kjeller, Norway.
- Magotra, N., N. Ahmed, and E. Chael (1987). Seismic event detection and source location using single-station (three-component) data, *Bull. Seism. Soc. Am.* **77**, 958–971.
- Mims, C. H. and R. L. Sax (1965). Rectilinear motion direction (REMODE), AD-460-631, Seismic Data Laboratory Report 118, Teledyne Geotech, Alexandria, Virginia.
- Montalbetti, J. F. and E. R. Kanasewich (1970). Enhancement of teleseismic body phases with a polarization filter, *Geophys. J. R. Astr. Soc.* **21**, 119–129.
- Mykkeltveit, S. and H. Bungum (1984). Processing of regional seismic events using data from small-aperture arrays, *Bull. Seism. Soc. Am.* **74**, 2313–2333.
- Oppenheim, A. V. and R. W. Schaffer (1975). *Digital Signal Processing*, Prentice-Hall, Englewood Cliffs, New Jersey.
- Ringdal, F. (1986). Regional event detection using the NORESS array, in *Proc. DARPA/AFGL Seismic Research Symposium*, May 6–8, pp. 102–109.
- Samson, J. C. and J. V. Olson (1980). Some comments on the descriptions of the polarization states of waves, *Geophys. J. R. Astr. Soc.* **61**, 115–130.
- Samson, J. C. and J. V. Olson (1981). Data-adaptive polarization filters for multichannel geophysical data, *Geophysics* **46**, 1423–1431.
- Simons, R. S. (1968). A surface-wave particle motion discrimination process, *Bull. Seism. Soc. Am.* **58**, 629–638.

- Smart, E. (1977). A three-component single-station maximum-likelihood surface wave processor, SDAC-TR-77-14, Teledyne, Geotech, Alexandria, Virginia.
- Smart, E. and H. Sproules (1981). Regional phase processors, SDAC-TR-81-1, Teledyne Geotech, Alexandria, Virginia.
- Sutton, G. A., J. A. Carter, and N. Barstow (1987). Source depths utilizing broad band data, Technical Report by Roundout Associates, Incorporated, Stone Ridge, New York.
- Von Seggern, D. and M. Marshall (1982). Definition of seismic signal parameters by particle-motion processing, SDAC-TR-81-19, Teledyne Geotech, Alexandria, Virginia.

CENTER FOR SEISMIC STUDIES
1300 N 17TH STREET, SUITE 1450
ARLINGTON, VIRGINIA 22209

Manuscript received 3 November 1987